I. A. S. Larsson
e-mail: sofia.larsson@ltu.se

E. M. Lindmark

T. S. Lundström

Division of Fluid Mechanics,
Luleå University of Technology,
SE-97187 Luleå, Sweden

G. J. Nathan
School of Mechanical Engineering,
University of Adelaide,
Adelaide, Australia

Secondary Flow in Semi-Circular Ducts

Turbulent secondary flows are motions in the transverse plane, perpendicular to a main, axial flow. They are encountered in non-circular ducts and can, although the velocity is only of the order of 1–3% of the streamwise bulk velocity, affect the characteristics of the mean flow and the turbulent structure. In this work, the focus is on secondary flow in semi-circular ducts which has previously not been reported. Both numerical and experimental analyses are carried out with high accuracy. It is found that the secondary flow in semi-circular ducts consists of two pairs of counter rotating corner vortices, with a velocity in the range reported previously for related configurations. Agreement between simulation and experimental results are excellent when using a second moment closure turbulence model, and when taking the experimental and numerical uncertainty into account. New and unique results of the secondary flow in semi-circular ducts have been derived from verified simulations and validating laser-based experiments.
[DOI: 10.1115/1.4004991]

Keywords: turbulent secondary flow, semi-circular duct, CFD, LDV

1 Introduction

Secondary flows are a mean flow in the transverse plane superimposed upon the axial mean flow and are generated and maintained by one of two fundamentally different mechanisms. The first occurs in curved ducts and is pressure driven, and the second is turbulence driven and is found in non-circular straight ducts. Prandtl formally separated these two categories into what is now known as secondary motions of Prandtl's first and second kind, respectively [1].

The first kind that originates from bent ducts can also in laminar flow have fairly large relative velocities, of the order of 20–30% of the bulk streamwise velocity. This type of flow has been extensively studied for a number of cases, (i.e. Shimizu et al. [2], Liou et al. [3], Westra et al. [4] and Flack and Brun [5]), and is dissipated within a straight circular duct. The second kind, encountered in non-circular ducts, is present also under fully developed conditions, and is caused by turbulence. The velocity is, in this case, only of the order of 1–3% of the streamwise bulk velocity, but may nevertheless profoundly affect the characteristics of the mean flow field as well as the turbulent structure. High momentum fluid is transported towards the corners, resulting in the bulging of the velocity contours and an increase of wall shear stress there. This effect is important for sediment transport and erosion problems, and it also affects the heat transfer and friction coefficient at duct walls [6].

This article focuses on the turbulence driven secondary flow of Prandtl's second kind in general, and on the secondary flow in semi-circular ducts in particular. The motivation for this is an ongoing study of the aerodynamics of a rotary kiln, and especially the kiln hood. A large part of the combustion air is introduced to the kiln through ducts with complex geometries; this results in a non-parallel and disordered flow which affects the mixing, and hence the combustion process. The details of the aerodynamics vary significantly from kiln to kiln and can have a significant impact on combustion performance [7].

One of the inlet ducts to the pellet kilns of interest here is close to semi-circular in cross-section; hence the focus of this work. In contrast to the considerable research on turbulent flows in square, rectangular and triangular ducts, an extensive literature search revealed no work on turbulent flow in semi-circular geometries. Both simulations and experiments have been performed in order to map the features of secondary flows. A review of turbulent secondary flow can be found in Bradshaw [8]. Square ducts have been investigated by Rung et al. [9], Petterson Reif and Andersson [1], and Kook Myong [10] to mention a few. Common for References [1,9,10] are that they consider limiting modeling constraints, while for References [9] and [10] the effect from wall functions on the secondary flow is also scrutinized. Rectangular ducts, in conjunction with square ducts, have been investigated by Rapley [11], Demuren and Rodi [6], Brundrett and Baines [12], Nakayama et al. [13] and Gessner and Jones [14]. Brundrett and Baines, and Gessner and Jones performed experiments to validate their simulations and analytical solutions, while the others used previously performed experiments for validation. Melling and Whitelaw [15] performed thorough measurements of the secondary flow in a rectangular duct to provide experimental data for validation of simulations. Speziale [16], Fife [17] and Hague et al. [18] analytically examined the origin of secondary flow, the production and main mechanisms of it. Speziale also proved why ordinary two-equation turbulence models cannot predict a secondary flow, while second-order closure models can. In agreement with this finding, Raiesi et al. [19] found, by a numerical study, that linear turbulence models are not able to represent the secondary flow while non-linear turbulence models are. Hurst and Rapley [20], Demuren [21], and Aly et al. [22] experimentally examined turbulent flow in triangular geometries. Aly et al. also performed simulations which they validated with their own experimental results. Other geometries that have also been investigated in some of the above articles include trapezoidal, elliptical and rod bundle geometries. However, as already observed, no suitable data are available for semi-circular ducts. Hence the aim of the present investigation is to map the turbulent secondary flow in a duct of semi-circular cross-section.

2 Method

Computational Fluid Dynamics (CFD) simulations of the fully developed flow through a virtual model of a duct with an almost semi-circular cross-section are performed with the commercial code Ansys CFX 12.1 on very fine grids. The code uses a coupled

Contributed by the Fluids Engineering Division of ASME for publication in the JOURNAL OF FLUIDS ENGINEERING. Manuscript received May 2, 2011; final manuscript received August 26, 2011; published online October 4, 2011. Assoc. Editor: Mark F. Tachie.

solver based on the finite volume method [23]. The simulations are then validated with Laser Doppler Velocimetry (LDV) measurements of the flow through a physical model built from Plexiglas with an identical geometry. The cross-section has a width of the base of 94 mm and the height is 33 mm. The duct is 4000 mm long and the origin is at the center of the outlet plane with the positive z-direction upstream towards the inlet. The geometry, with the grid structure, can be seen in Fig. 1. Note that the grid used for the simulations is much finer than that presented in Fig. 1.

To achieve a fully developed velocity field, the duct has a length of 95 hydraulic diameters ($D_h = 0.042$ m) of the semi-circular duct both in the virtual and physical model. Dean and Bradshaw [24] obtained fully developed flow in a rectangular duct after 93.6 hydraulic diameters for $Re = 1 \times 10^5$ (based on the height of the duct).

2.1 Experimental Setup. Secondary flows are present in the mean flow and amenable for investigation with either LDV or PIV (Particle Image Velocimetry). The advantage of PIV is the planar measurement providing directly an understanding of two dimensional flow structures [25]. The dynamic velocity range and the spatial resolution, however, are poorer than for LDV. In conjunction with a large dynamic velocity range, a large dynamic spatial range is necessary to measure small scale variation embedded in large scale motion, such as flow in boundary layers and small scale turbulence or the flow in the transverse plane in a duct. Dynamic spatial range is related to spatial resolution, and dynamic velocity range is related to the fundamental velocity resolution and accuracy of PIV [26]. Velocities yielding a displacement under 0.1 pixels between exposures are tricky to capture [27]. Raffel [28] recommends a maximum particle displacement of 1/4 of the interrogation area between exposures to avoid loss of particle patterns. In Larsson et al. [29] the authors studied the same setup as focused on in this work and used an interrogation area of 32×32 pixels with a pixel displacement of 8 pixels between exposures. This means that with a transversal velocity with the magnitude of 1–3% of the main axial velocity, the particles move 0.08–0.32 pixels in the transversal direction between exposures. It is possible to measure velocities down to 0.02 pixels with reasonable PIV algorithms. The algorithm error is fixed in pixels, which means that if a maximum tolerable error is 10%, then the minimum resolvable displacement is 0.2 pixels [30]. Hence to obtain a good enough resolution of the small transversal velocity field LDV was chosen in this study.

Another main reason for using LDV instead of PIV is the optical limitation of the experimental arrangement. The setup has been optimized to investigate the main flow in the axial direction and hence it is difficult to directly perform PIV measurements in the transversal plane.

To control the flow rate in the semi-circular duct, the flow was monitored with a magnetic flow meter (Krohne Optiflux DN50, error 0.1%). The temperature of the water was controlled to 22 ± 0.4 °C with the aid of a cooling system in the tank. The supply pipe to the semi-circular duct was achieved through a transition piece, whose diameter matched the base of the semi-circular section to provide a flush interface along the circular surface and an abrupt transition at the base. The inlet to the transition piece was fed via smaller pipes oriented normal to the axis of the semi-circular section. The outlet transition piece was identical, but oriented in the opposite direction.

The LDV-system used was a commercially available system from Dantec. It is a two component configuration with an 85 mm optical fiber probe and a front lens with a 310 mm focal length. The system consists of a 20 W continuous wave Argon-Ion laser, transmitting optics including a beam splitter Bragg-cell, photodetectors and signal processors. The system was used in backscatter mode in combination with two Burst Spectrum Analyzers (BSA). The dimension of the measurement volume was approximately $0.074 \times 0.074 \times 0.63$ mm for both colors when measured in air. The water was seeded with polyamide particles with a diameter of 5 μm (Dantec's PSP-5). Dantec's BSA Flow software with the burst mode spectrum analysis method was used for the data acquisition. The 2D-LDV probe was placed on a traversing mechanism controlled by the software, with a possible smallest step of 0.01 mm. The sampling time was set to 240 s or 900 s at each measurement point and for each direction. The measurement time corresponded to at least 10,000 samples and was dependent on the location of the measuring point.

Two mass flows were investigated, 3.95 kg/s and 0.395 kg/s corresponding to Reynolds number of 8×10^4 and 8×10^3, respectively, based on the hydraulic diameter. The turbulence intensity in the inlet duct was approximately 6%.

Due to the optical limitations of the measuring section, the two secondary flow components were measured from two different directions. The experimental arrangement can be seen in Fig. 2. First, the probe was mounted facing the plane surface and the y-direction (position A) and measuring the main, axial component and the velocity in the x-direction. After that the probe was mounted beside the channel, facing the x-direction (position B) and measuring once again the main, axial velocity component and the component in the y-direction. When measuring from the side of the channel, the measurements are distorted by the optical refraction due to the curved surface of the duct. To minimize this

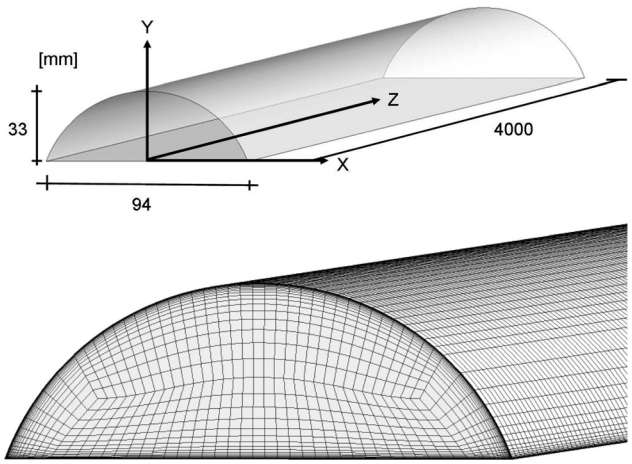

Fig. 1 Geometry with grid structure

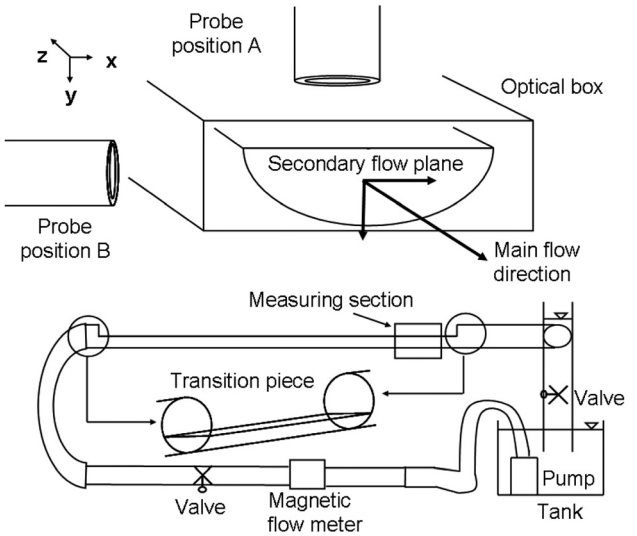

Fig. 2 Experimental arrangement

problem, the duct was placed in an optical measuring box filled with water.

Generally, the experimental challenges increase with optical path length through the apparatus, especially through the curved wall. The worsening of the optical condition is related to the optical aberration and the dislocation of laser beam waists. This optical aberration implies that the larger the path length through the flow, the fewer the effective elementary segments on the receiving lens; this results in a deterioration of the velocity signals and thus in the decrease of the signal rate. For this reason, it is unrealistic to obtain velocity signals of sufficiently high quality for optical depths greater than two-thirds of the pipe diameter. The entire flow distribution can therefore only be achieved if an additional measurement is carried out from the opposite side by rotating the LDV system 180° around the pipe axis [31]. Also, when traversing the laser beams towards the circular part, one can exhibit "blind regions" due to the total reflection of the laser beams at the inner walls. This leads to some missing experimental data in the central, circular part of the duct. The only way to remove the blind regions, where LDV measurements cannot be performed, is to perfectly match the refractive index of the fluid to that of the duct which was judged not to be necessary here. In addition to the blind regions, both laser beams will have different intensities away from the duct center, resulting in a lower depth of modulation of the interference field, and therefore in lower values of the signal-to-noise ratio [32]. Since the four beams do not intersect in a single point due to the optical aberration of the circular surface, velocity measurements were not performed in coincidence mode for the cases with the beams passing through the curved surface. Measurements through the flat surface were straightforward and performed in coincidence mode.

The total uncertainty in the measurements is a combination of systematic (bias) and random (precision) errors [33]. The bias errors in LDV measurements are the calibration factor, probe alignment/configuration bias, velocity bias and system noise. The system was carefully set up to minimize bias errors, so that the main contributors to bias errors considered in this paper are velocity bias and system noise.

In LDV measurements, the sample rate of the velocity increases with velocity. For a given observation time, higher velocities will be sampled more frequently than lower velocities. Taking a simple arithmetic mean of all samples thus leads to a positively biased mean compared to a true time mean of the velocity [34]. This was compensated for by weighting each velocity sample with its residence time in the measuring volume.

The system noise originates from vibrations of the test setup, leading to a small movement of the duct wall. The system noise was estimated by a velocity measurement of the duct wall in the measuring section, with the same hardware settings as for the flow measurements. The measured noise contribution to the velocities was subtracted from the velocity data.

The precision error was estimated by a repeatability test. Measurements at five different points were performed ten times in a randomized order. The estimated precision error (P) of the mean values, at the probability of 95% confidence interval, was calculated with the following relationship $P = t \times s$, where t is the coefficient of the t-distribution with the corresponding degree of freedom and s is the standard deviation of the sample data [33]. The overall estimated uncertainty of the secondary velocity measurements was between 1-5%, with the higher values occurring close to the walls.

2.2 CFD Methodology. The geometry was imported into Ansys ICEM and a curvilinear grid was built from hexahedral elements. An o-grid was designed in order to get a good grid adaptation around the curved edges. The grid was also designed to meet the good quality grid criterion provided by the code [23] in order to reduce the discretization error. The overall grid structure can be seen in Fig. 1. To resolve the boundary layer, prism elements were placed close to the wall. This results in better modeling of the near-wall physics.

The turbulent flow field was solved by three dimensional, steady state, Reynolds averaged Navier-Stokes (RANS) equations, closed by either the two-equation Shear Stress Transport (SST) turbulence model or the Reynolds stress Baseline (BSL) turbulence model. The choice of turbulence models emanates from the initial literature review where the conclusion was that a Reynolds stress model without wall functions is necessary to predict turbulent secondary flow. From the available RANS turbulence models in Ansys CFX which meets these criterions, the Reynolds stress model BSL was chosen since it is based on the same hybrid model as the two-equation model SST. This facilitates the simulation work since the same grid can be used in all simulations, regardless of turbulence model. The two-equation model SST was used in order to confirm that standard two-equation turbulence models cannot show turbulent secondary flow without modification of the model.

The SST turbulence model originates from the $k-\omega$ formulation by Wilcox [35]. The Wilcox model has the disadvantage of a strong sensitivity to free stream conditions. This can be avoided by combining the $k-\omega$ model near the surface with the $k-\varepsilon$ model in the outer region, which is the base for the SST model. Another advantage of the SST model (compared with other hybrid models) is its capability of properly predicting the onset and amount of flow separation from smooth surfaces under adverse pressure gradients. This is due to the fact that the model accounts for transport of turbulent shear stress by introducing an eddy viscosity limiter [36].

The BSL Reynolds stress model is a turbulence model which uses the ω-equation instead of the ε-equation as the scale-determining equation. One of the advantages of the ω-formulation is the near wall treatment for low-Reynolds number computations, where it is more accurate and more robust. As the free stream sensitivity of the standard ω-model does carry over to the Reynolds stress model, the BSL Reynolds stress model is based on the ω-equation used in the BSL two-equation model (which is basically the SST model without the eddy viscosity limiter needed in order to account for the transport of the turbulent shear stress). A separate transport equation must be solved for each of the six Reynolds stress components [23].

Turbulence-induced secondary flows are driven by the difference of the normal Reynolds stresses perpendicular to the principal velocity [9]. Because of Boussinesq's linear (isotropic) eddy-viscosity hypothesis, which does not account for turbulence anisotropy, standard two-equation models cannot reveal a secondary flow [1]. This is also shown in the present study. Due to this fact, most results are taken from simulations using the Reynolds stress turbulence model. Since regions close to the wall and the corners are known to influence the characteristics of secondary flow significantly, wall function formulations should be avoided [21]. This explains the choice of turbulence models used in the present study.

A mass flow plug profile is set at the inlet, with a turbulence intensity of 5%. The sensitivity of the result to an increased level of turbulence intensity (8%) was tested, showing no difference in important variables. At the outlet, an average static pressure is employed with a relative pressure of zero Pa, averaged over the whole outlet. This allows the outlet pressure to vary based on upstream influences. The walls are specified as no slip walls. A formally second order accurate discretization scheme is used for the advection term. The convergence criterion is RMS residuals below 10^{-6} [29] and therefore double precision is used. The convergence criterion assures a decrease of at least three orders of magnitude of the normalized residual for each equation solved. Isothermal conditions are assumed so the energy equations are not applied. The simulations are mainly carried out on a 150-node PC-cluster. It has been demonstrated that the CFD-code applied on this cluster parallelize excellently [37].

A grid study was performed to estimate the discretization error. The dependent variable chosen to study was the x-component of

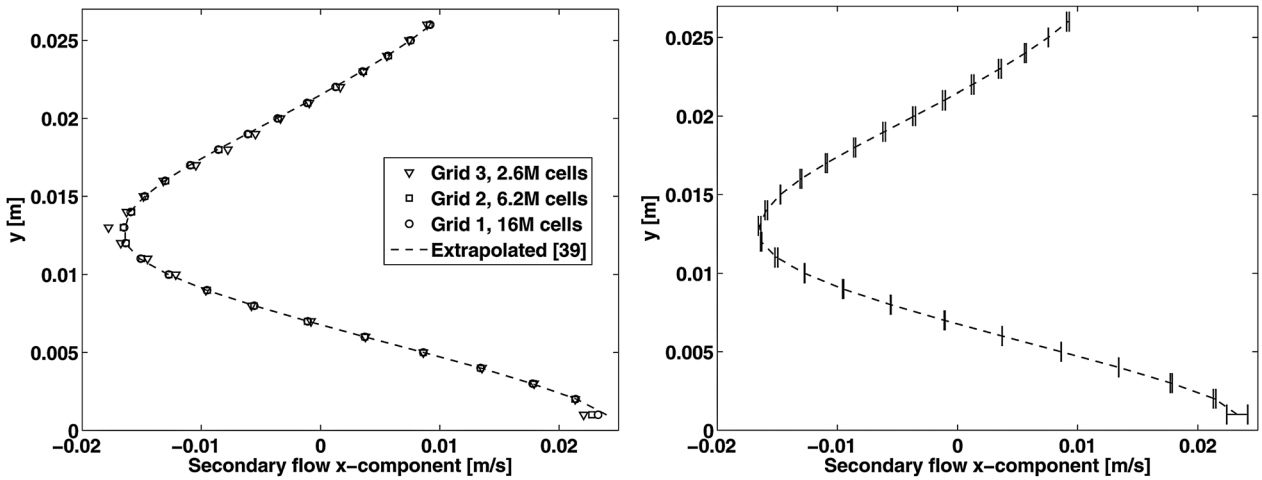

(a) Secondary flow x-component velocity profile

(b) Fine-grid solution with discretization errorbars

Fig. 3 The sensitivity of the calculated flows to grid refinement, showing velocity profiles at $x = -20$ mm, $Re = 8 \times 10^4$, using the BSL-model

the secondary flow along a line located at $x = -20$ mm. Since the secondary flow velocity is small the velocity difference between two grids is small, and hence the solution was normalized with its range [38]. The three grids chosen had approximately 2.6×10^6, 6.2×10^6 and 16×10^6 elements, respectively. The Richardson extrapolation [39] was performed with a grid refinement factor of approximately 1.35. The global average calculated apparent order was 1.75. Oscillatory convergence occurred at 5 out of 27 points. Figure 3 shows the velocity profiles and the fine-grid solution along with discretization errorbars assessed with the Grid Convergence Index (GCI) values. The maximum discretization uncertainty was approximately 10%, corresponding to a maximum uncertainty in velocity of about $\pm$ 1.2×10^{-4} m/s. The average discretization uncertainty of the fine-grid solution based on the GCI value was 1.8%.

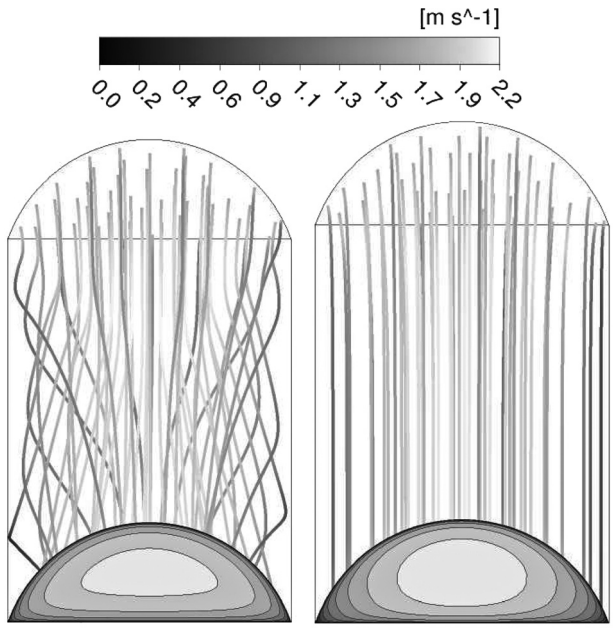

(a) Reynolds stress model BSL (b) Two-equation model SST

Fig. 4 Calculated axial flow contours with streamlines of the main, axial flow from inlet to outlet of the duct. Simulations were performed with Reynolds stress model BSL (left) and SST turbulence model (right). $Re = 8 \times 10^4$.

The simulation results reported below are from the grid consisting of 16×10^6 elements. The y^+ values are in the range of 0.005 to 1.3, with an area averaged maximum value of 0.38. The maximum y^+ value of 1.3 is only located close to the inlet to the duct so the boundary layer is fully resolved everywhere throughout the geometry according to the requirements of low-Re wall formulations for an ω-based turbulence model [23]. This means that there are no wall functions which would impair the prediction of the secondary flow.

3 Results and Discussion

A qualitative comparison between simulations and experiments is presented first, followed by a quantitative comparison. Due to the complexity of the measurements through the curved surface of the duct, the errors in measuring the y-component of the secondary flow are greater than those in the x-direction. The focus is therefore on comparing the x-component of the simulation and experimental results. If not stated otherwise, the simulation results are presented for the BSL Reynolds stress turbulence model.

The first indication of the existence of secondary flow is distortion of the axial flow contours for flow in the streamwise direction. If secondary flows are present, the axial flow contours will bulge out towards the corners, as can be seen in Fig. 4(*a*) for the simulation using the BSL model and in Fig. 5 for the experimental result. No secondary flow is found for the SST model (Fig. 4(*b*)).

Helical streamlines of the axial flow is another indication of secondary flow. Figure 4 also shows the streamlines along the duct for the simulated results. Notice that for the SST turbulence model, the streamlines are straight.

Simulations with the BSL Reynolds stress turbulence model further revealed that the secondary flow consists of two pairs of counter rotating corner vortices with the flow convected into the

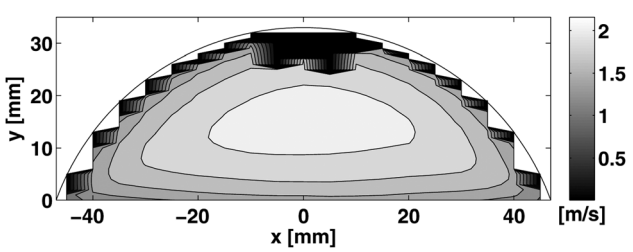

Fig. 5 Measured axial flow contours, $Re = 8 \times 10^4$, obtained at $z/D_h = 92$

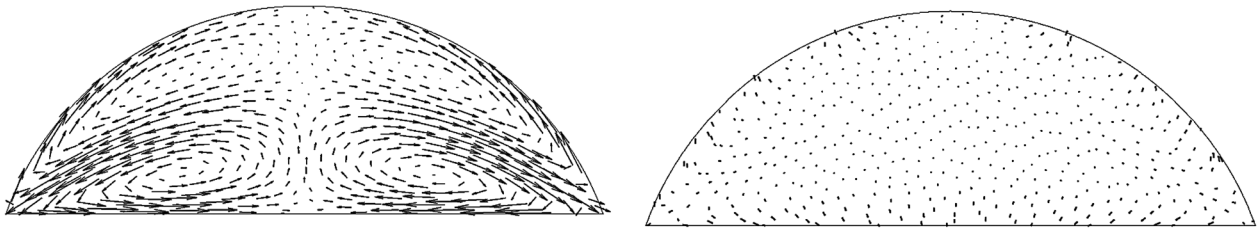

(a) Reynolds stress model BSL

(b) Two-equation model SST

Fig. 6 Secondary flow in the semi-circular duct, calculated with a Reynolds stress model (BSL) to the left, a standard two-equation model (SST) to the right. $Re = 8 \times 10^4$.

corners from the central region and away from the corners along the walls (Fig. 6(*a*)). The vorticity distribution that results from the rotational flow in Fig. 6(*a*) is rather symmetrical and decays towards the symmetry line of the cross-section, see Fig. 7. Once again, the standard two-equation models do not capture secondary flow, as shown in Fig. 6(*b*).

A comparison of the *x*-component of the secondary flow between the simulation and experimental results reveals good qualitative agreement and confirms the characteristics of the secondary flow presented above (Fig. 8(*a*)–8(*b*)). The measured flow distribution is obviously not as well resolved as the simulated case, but the main flow features are the same and the magnitudes of the simulated and measured velocities are in the same range, with the maximum being about 1.5% of the bulk velocity, U_{bulk}, for both cases. When repeating the measurements at a cross-section upstream ($z/D_h = 88$), a small difference in velocity field was detected, as can be seen when comparing Fig. 8(*b*) with Fig. 8(*c*). The patterns agree but the locations of the contours differ somewhat. Notice that the simulation results overlap perfectly at these two cross-sections so that the simulated results at $z/D_h = 88$ are identical to Fig. 8(*a*).

There is also good qualitative agreement between the simulated and measured values of the Reynolds normal stresses, with rather low stresses in boomerang-shaped areas in the middle of the duct, see Figs. 9–11. For the experimental case, only the normal stress of the *x*-component and the axial component are shown due to lack of data for the *y*-component.

The turbulent kinetic energy and corresponding intensity can be seen in Fig. 12 and Fig. 13. By comparing the simulation results from the Reynolds stress model BSL of Fig. 4(*a*) with Fig. 12(*a*), especially in the corner regions, it is evident that the contours of the turbulent kinetic energy are more distorted than the mean axial flow contours. This indicates that the turbulence field is more disturbed by the secondary flow than is the mean velocity field, agreeing with Brundrett and Baines [12], Nakayama et al. [13] and Aly et al. [22]. The same trend is found in the experimental results when comparing Fig. 5 with Fig. 12(*b*).

The anisotropy of the normal stresses ($\tau_{xx} - \tau_{yy}$) is shown in Fig. 14 for the simulation result only, since the secondary velocity components are not correlated in the experiment. The secondary shear stress acting in the cross-sectional plane (τ_{xy}) can also be seen in Fig. 14. The gradients of the above stresses are the leading cause of secondary flow motions [12].

A lower Reynolds number case was also assessed to investigate the Reynolds number influence on the secondary flow. The basic pattern of the secondary flow is independent of Reynolds number, agreeing with the results obtained by Brundrett and Baines [12], as shown in Fig. 8(*d*). The non-dimensionalized secondary flow

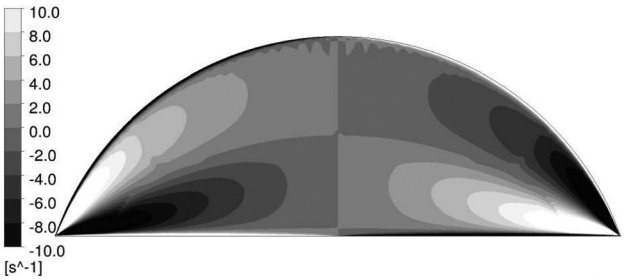

Fig. 7 Vorticity contour plot, simulation result with $Re = 8 \times 10^4$.

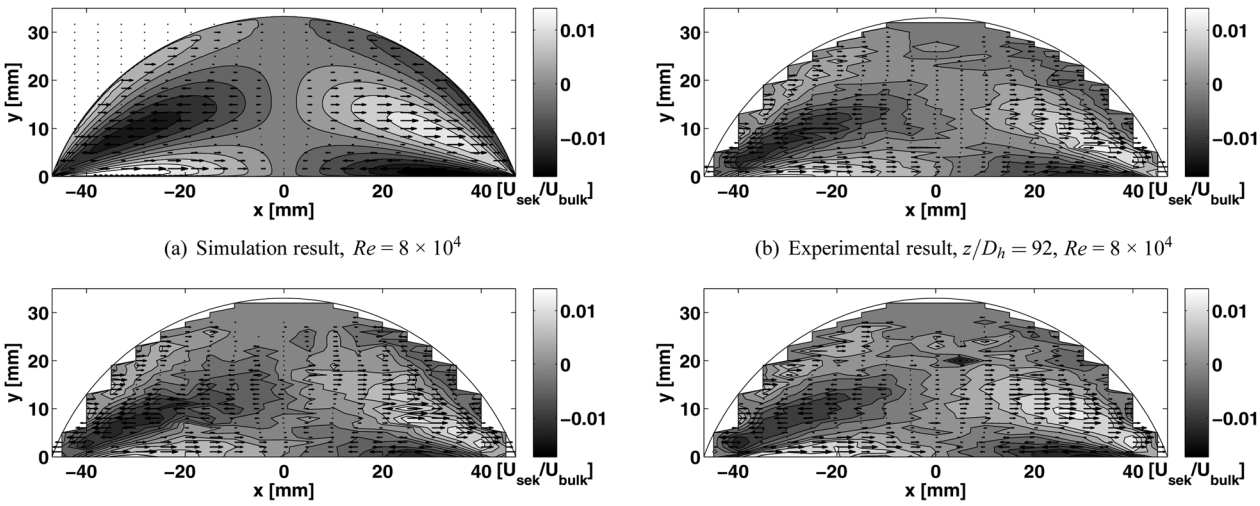

(a) Simulation result, $Re = 8 \times 10^4$

(b) Experimental result, $z/D_h = 92$, $Re = 8 \times 10^4$

(c) Experimental result, $z/D_h = 88$, $Re = 8 \times 10^4$

(d) Experimental result, $z/D_h = 92$, $Re = 8 \times 10^3$

Fig. 8 Vector and contour plots of the *x*-component of the secondary flow

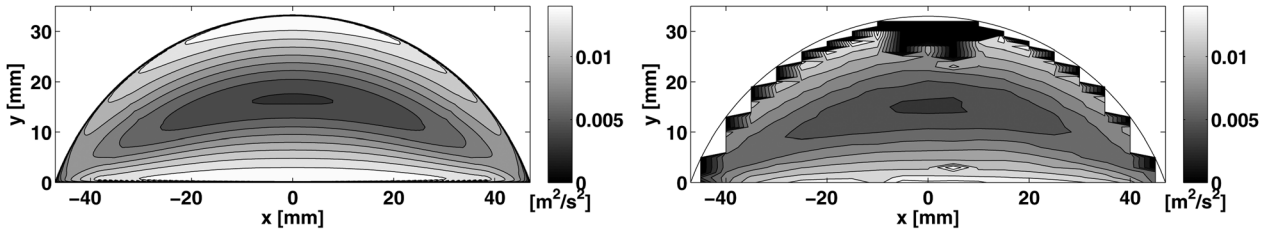

(a) Simulation (b) Experiment, $z/D_h = 92$

Fig. 9 Reynolds normal stress τ_{xx}. Simulation results to the left, experimental results to the right. $Re = 8 \times 10^4$.

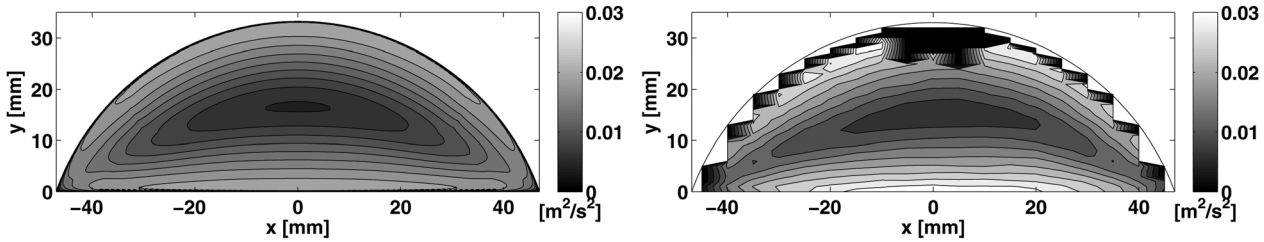

(a) Simulation (b) Experiment, $z/D_h = 92$

Fig. 10 Reynolds normal stress τ_{zz}. Simulation results to the left, experimental results to the right. $Re = 8 \times 10^4$.

velocities are also similar (a maximum velocity of approximately 1% of the axial flow) in the experimental case while they perfectly match in the simulation results. Another observation by Brundrett and Baines was that, with increasing values of Reynolds number, the flow penetrates farther into the corners and approaches the wall more. Gessner and Jones [14] found that the non-dimensionalized secondary flow velocities decreased with an increase of Reynolds number. They suggested that this effect may be explained by increased turbulent mixing at high Reynolds number, which tends to decrease gradients in the flow. Neither of these observations can be seen in the present study. A more thorough investigation of the Reynolds number dependency is therefore warranted.

The quantitative comparison between simulation and experimental results for $Re = 8 \times 10^4$ is based on the numerical uncertainty assessed with the GCI index approach and the estimated experimental uncertainties. Presented here is the secondary flow component, defined as the x-velocity. Four lines are chosen, reporting results from evenly spread locations in one half of the semi-circular duct due to symmetry. The results are presented with errorbars corresponding to the average discretization uncertainty for the simulation case and the average experimental uncertainty, and can be seen in Fig. 15.

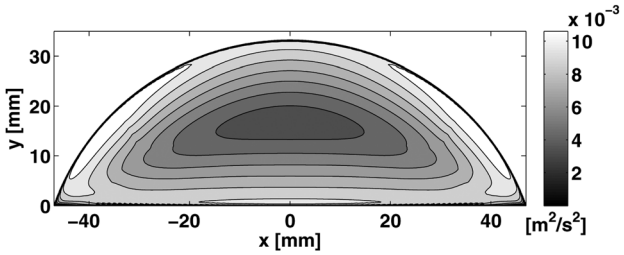

Fig. 11 Reynolds normal stress τ_{yy}, simulation results with $Re = 8 \times 10^4$

Overall, the quantitative agreement between simulation and experiment is good, although there are significant differences between the two in some cases. One common feature of the profiles is that the deviation increases with optical path length and when approaching the curved surface. As described above, the velocity signal deteriorates with increasing optical path length, leading to a decrease in signal rate and hence also in signal-to-noise ratio. Reflections also affect the signal quality and can lead to measurement errors. The reflections become more prominent closer to the corner, increasing errors. The apparently large deviations between simulation and experimental results along the profile at $x = 5$ mm (Fig. 15(*a*)) stems from the fact that the secondary flow velocity is very close to zero, making small velocity differences result in large % deviations. This should be kept in mind when comparing the results quantitatively. The experimental results also indicate that the highest velocities are found close to the wall, supporting the previously reported conclusions that wall functions should be avoided when simulating the turbulent secondary flow in a non-circular duct.

Finally, there should be some comment regarding the y-component of the secondary flow. A qualitative comparison between

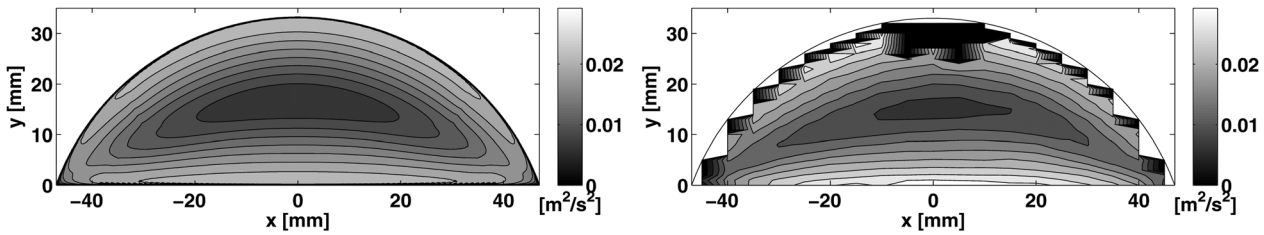

(a) Simulation (b) Experiment, $z/D_h = 92$

Fig. 12 Contour plot of turbulent kinetic energy. Simulation results to the left, experimental results to the right. $Re = 8 \times 10^4$.

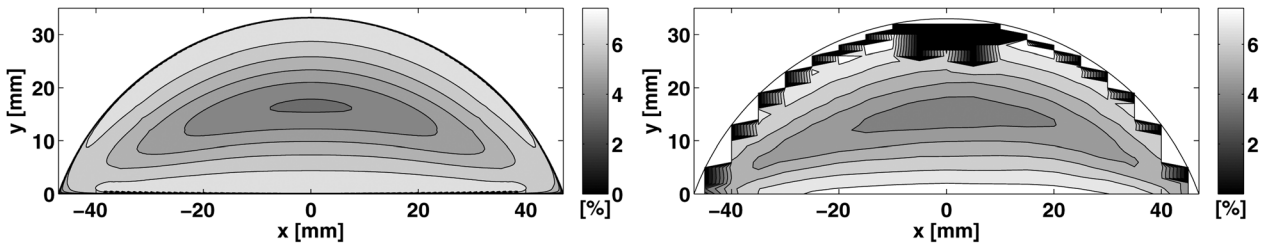

(a) Simulation (b) Experiment, $z/D_h = 92$

Fig. 13 Contour plot of turbulence intensity. Simulation results to the left, experimental results to the right. $Re = 8 \times 10^4$.

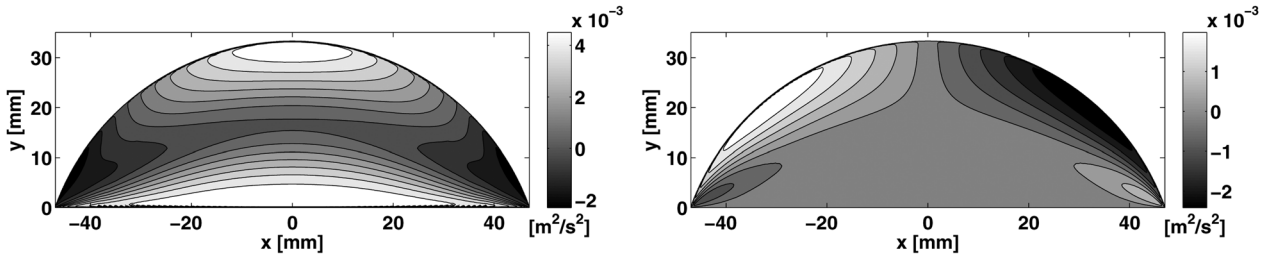

(a) $\tau_{xx} - \tau_{yy}$ (b) τ_{xy}

Fig. 14 Anisotropy of the normal stresses ($\tau_{xx} - \tau_{yy}$) to the left, Reynolds shear stress (τ_{xy}) to the right. Simulation results with $Re = 8 \times 10^4$.

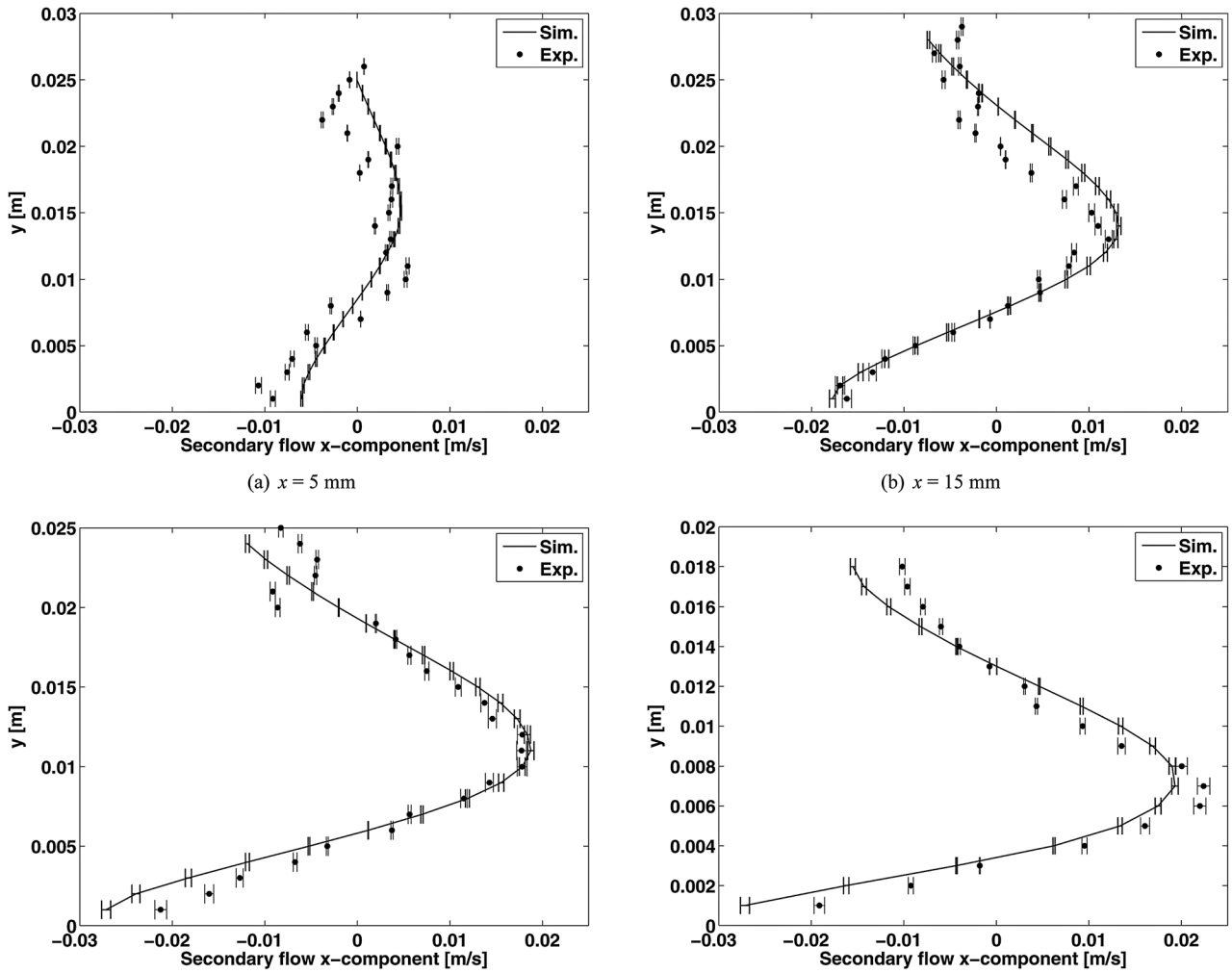

(a) $x = 5$ mm (b) $x = 15$ mm

(c) $x = 25$ mm (d) $x = 35$ mm

Fig. 15 Velocity profiles, a comparison of the simulated and experimental data (obtained at $z/D_h = 92$), at $Re = 8 \times 10^4$

simulation and experimental results in the measurable part of the duct shows good agreement also in the direction of the *y*-component. As outlined earlier, the experimental result should be treated with caution since no correction for either the position of the measurement volume or the velocity has been made.

4 Summary and Conclusions

The turbulent secondary flow in a semi-circular duct was investigated both numerically with a commercially available code and experimentally with Laser Doppler Velocimetry, yielding new results. The secondary flow in semi-circular geometries consists of two pairs of counter rotating corner vortices. The maximum magnitude of the secondary velocity is about 1% of the streamwise bulk velocity. Qualitative comparisons in the secondary flow plane between simulations with a Reynolds stress turbulence model and experiments show agreement as to velocities and Reynolds normal stresses. The main features found in studies on similar geometries are captured. The results indicate that the turbulence field is more disturbed by the secondary flow than is the mean velocity field.

A quantitative comparison of the velocity along four transverse profiles show good overall agreement, with increased deviations between simulation and experiment when approaching the curved surface. When comparing the results quantitatively, it should be kept in mind that the secondary flow velocity is very close to zero, making small velocity differences result in large % deviations. It should also be noted that the highest velocities are found close to the wall, implying that wall functions should be avoided when modeling the turbulent secondary flow. Standard two-equation turbulence models should also be avoided since they fail to predict any turbulent secondary flow.

Acknowledgment

This work was carried out within the framework of the Faste Laboratory, a VINNOVA Excellence Centre. The authors also acknowledge discussions with LKAB, who also partly financed the work via the Faste Laboratory. A special thanks to Mr. Berhanu Mulu, Division of Fluid Mechanics, Luleå University of Technology for valuable help with the LDV-measurements.

References

[1] Petterson, R. B., and Andersson, H., 2002, "Prediction of Turbulence-Generated Secondary Mean Flow in a Square Duct," Flow, Turbul. Combust., **68**, pp. 41–61.
[2] Shimizu, Y., Futaki, Y., and Martin, C. S., 1992, "Secondary Flow and Hydraulic Losses within Sinuous Conduits of Rectangular Cross Section," J. Fluids Eng., **114**, pp. 593–600.
[3] Liou, T.-M., Chen, C.-C., and Chen, M.-Y., 2003, "Rotating Effect on Fluid Flow in Two Smooth Ducts Connected by a 180-Degree Bend," J. Fluids Eng., **125**, pp. 138–148.
[4] Westra, R., Broersma, L., van Andel, K., and Kruyt, N., 2010, "PIV Measurements and CFD Computations of Secondary Flow in a Centrifugal Pump Impeller," J. Fluids Eng., **132**, pp. 0611041–0611048.
[5] Flack, R., and Brun, K., 2005, "Fundamental Analysis of the Secondary Flows and Jet-Wake in a Torque Converter Pump - Part II: Flow in a Curved Stationary Passage and Combined Flows," J. Fluids Eng., **127**, pp. 75–82.
[6] Demuren, A., and Rodi,W., 1984, "Calculation of Turbulence-Driven Secondary Motion in Non-Circular Ducts," J.Fluid Mech., **140**, pp. 189–222.
[7] Mullinger, P., and Jenkins, B., 2008. *Industrial and Process Furnaces: Principles, Design and Operation*, 1st ed. Butterworth-Heinemann, Oxford, UK.
[8] Bradshaw, P., 1987, "Turbulent Secondary Flows," Annu. Rev. Fluid Mech., **19**, pp. 53–74.
[9] Rung, T., Lübcke, H., Thiele, F., Fu, S., Wang, C., and Guo, Y., 2000, "Turbulence Closure Model Constraint Derived from Stress-Induced Secondary Flow," AIAA J., **38**(9), pp. 1756–1758.
[10] Kook Myong, H., 1991, "Numerical Investigation of Fully Developed Turbulent Fluid Flow and Heat Transfer in a Square Duct," Int. J. Heat Fluid Flow, **12**(4), December, pp. 344–352.
[11] Rapley, C., 1982, "The Simulation of Secondary Flow Effects in Turbulent Non-Circular Passage Flows," Int. J. Numer. Methods Fluids, **2**, pp. 331–347.
[12] Brundrett, E., and Baines, W., 1964, "The Production and Diffusion of Vorticity in Duct Flow," J. Fluid Mech., **19**, pp. 375–394.
[13] Nakayama, A., Chow, W., and Sharma, D., 1983, "Calculation of Fully Developed Turbulent Flows in Ducts of Arbitrary Cross-Section," J. Fluid Mech., **128**, pp. 199–217.
[14] Gessner, F., and Jones, J., 1965, "On Some Aspects of Fully-Developed Turbulent Flow in Rectangular Channels," J. Fluid Mech., **23**(4), pp. 689–713.
[15] Melling, A., and Whitelaw, J., 1976, "Turbulent Flow in a Rectangular Duct," J. Fluid Mech., **78**(2), pp. 289–315.
[16] Speziale, C., 1982, "On Turbulent Secondary Flows in Pipes of Noncircular Cross-Section," Int. J. Eng. Sci., **20**(7), pp. 863–872.
[17] Fife, P., 1992, "Geometrical Aspects of Secondary Motion in Turbulent Duct Flow," Theor. Comput. Fluid Dyn., **4**, pp. 51–70.
[18] Haque, M., Hassan, A., Turner, J., and Barrow, H., 1983, "An Observation on the Origin of Secondary Flow in Straight Noncircular Ducts," Int. J. Heat Mass Transfer, **17**, pp. 93–95.
[19] Raiesi, H., Piomelli, U., and Pollard, A., 2011, "Evaluation of Turbulencemodels using Direct Numerical and Large-Eddy Simulation Data," J. Fluids Eng., **133**, pp. 021203–021212.
[20] Hurst, K., and Rapley, C., 1991, "Turbulent Flow Measurements in a 30/60 Degree Right Triangular Duct," Int. J. Heat Mass Transfer, **34**(3), pp. 739–748.
[21] Demuren, A., 1991, "Calculation of Turbulence-Driven Secondary Motion in Ducts with Arbitrary Cross Section," AIAA J., **29**(4), pp. 531–537.
[22] Aly, A., Trupp, A., and Gerrard, A., 1978, "Measurements and Prediction of Fully Developed Turbulent Flow in an Equilateral Triangular Duct," J. Fluid Mech., **85**(1), pp. 57–83.
[23] Ansys CFX, 2009, *Ansys CFX-Solver Theory Guide,* Elsevier Academic Press. Release 12.1.
[24] Dean, R., and Bradshaw, P., 1976, "Measurements of Interacting Turbulent Shear Layers in a Duct," J. Fluid Mech., **78**(4), pp. 641–676.
[25] Hyun, B., Balachandar, R., Yu, K., and Patel, V., 2003, "Assessment of PIV to Measure Mean Velocity and Turbulence in Open-Channel Flow," Exp. Fluids, **35**, pp. 262–267.
[26] Adrian, R., 1997, "Dynamic Ranges of Velocity and Spatial Resolution of Particle Image Velocimetry," Meas. Sci. Technol., **8**, pp. 1393–1398.
[27] Lavoie, P., Avallone, G., Gregorio, F. D., Romano, G., and Antonia, R., 2007, "Spatial Resolution of PIV for the Measurement of Turbulence," Exp. Fluids, **43**, pp. 39–51.
[28] Raffel, M., Willert, C., Wereley, S., and Kompenhans, J., 2007, *Particle Image Velocimetry: A Practical Guide*, 2nd ed., Springer-Verlag, Berlin Heidelberg.
[29] Larsson, S., Lindmark, E., Lundström, S., Marjavaara, D., and Töyrä, S., 2013, "Visualization of Merging Flow by Usage of PIV and CFD with Application to Grate-Kiln Induration Machines," J. App. Fluid Mech., Accepted for publication.
[30] Spedding, G., 2009, "PIV-Based Investigations of Animal Flight," Exp. Fluids, **46**, pp. 749–763.
[31] Zhang, Z., 2004, "Optical Guidelines and Signal Quality for LDA Applications in Circular Pipes,". Experiments in Fluids, **37**, pp. 29–39.
[32] Gardavský, J. Hrbek, J. Chára, Z. and Severa, M., 1989, "Refraction Corrections for LDA Measurements in Circular Tubes within Rectangular Optical Boxes," Laser Anemom., Dantec Information, **8**.
[33] Coleman, H., and Steele, W., 1999, *Experimentation and Uncertainty Analysis for Engineers*, 2nd ed. John Wiley & Sons, New York.
[34] Albrecht, H.-E., Borys, M., Damaschke, N., and Tropea, C., 2003, *Laser Doppler and Phase Doppler Measurement Techniques*. Springer Verlag, Berlin Heidelberg.
[35] Wilcox, D., 1986, "Multiscalemodel for Turbulent Flows," *In AIAA 24th Aerospace ScienceMeeting*, American Institute of Aeronautics and Astronautics.
[36] Menter, F., 1993, "Multiscale Model for Turbulent Flows," *In 24th Fluid Dynamics Conference*, American Institute of Aeronautics and Astronautics.
[37] Hellström, G. Marjavaara, D., and Lundström, S., 2007, "Redesign of a Hydraulic Turbine Draft Tube with Aid of High Performance Computing," Adv. Eng. Software, **38**(5), pp. 338–344.
[38] Coleman, H., and Stern, F., 1997, "Uncertainties and CFD Code Validation," J. Fluids Eng., **119**, pp. 795–803.
[39] Celik, I., Ghia, U., Roache, P, and Freitas, C., 2008, "Procedure for Estimation and Reporting of Uncertainty Due to Discretization in CFD," J. Fluids Eng., **130**, pp. 338–344.